Revision 1; Word Count: 11048

Repeat, fast and high-resolution mapping of fine-scale trace element distribution in pyrite and marcasite by LA-Q-ICP-MS with the Aerosol Rapid Introduction System (ARIS)

Merilie A. Reynolds[1a*], Balz S. Kamber[2,3], Cora A. McKenna[2], Marcus Oelze[4], and Sarah A. Gleeson[4,5]

[1] University of Alberta, Department of Earth and Atmospheric Sciences, Edmonton, Alberta, Canada

[2] Irish Centre for Research in Applied Geosciences, Department of Geology, School of Natural Sciences, Trinity College Dublin, Dublin 2, Ireland

[3] School of Earth and Atmospheric Sciences, Queensland University of Technology (QUT) | GPO Box 2434, Brisbane, QLD 4001, Australia

[4] GFZ, German Research Centre for Geosciences, 14473 Potsdam, Germany

[5] Institute of Geological Sciences, Freie Universität Berlin, Malteserstrasse, 74-100, Berlin, 12249, Germany

[a] Present address: Northwest Territories Geological Survey, Government of Northwest Territories, Yellowknife, Canada

* Correspondence: Merilie_Reynolds@gov.nt.ca

Abstract

The minor and trace element composition of minerals provides critical insights into a variety of geological processes. Multi-element mapping by laser ablation-inductively coupled plasma-mass spectrometry (LA-ICP-MS) is an important technique applied for this purpose and although the method is rapidly advancing, there remains a fundamental compromise between

spatial resolution, detection limit and experiment duration when using sequential mass analyzers. To address the limitation of limited analyte selection for high-spatial resolution maps imposed by the sequential nature of typical quadrupole (Q)-ICP-MS, we trialed the Aerosol Rapid Introduction System (ARIS) for repeat mapping of the same area. The ARIS is a high-speed transfer tubing system that reduces aerosol washout times, permitting resolution of individual pulses at 40-60 Hz. Here, the ARIS was tested not for pulse resolution but with novel operating conditions optimized to perform fast, high spatial resolution mapping of minor and trace element distribution in pyrite and marcasite. For this purpose, ablation was conducted with a 5 μm beam aperture, a repetition rate of 50 Hz, and a continuous stage scan speed of 40 μm s^{-1}. For each LA-Q-ICP-MS map, data was acquired for 6 elements with an acquisition time of 20 ms per element. This deliberately surrendered the individual pulse resolution of the ARIS but instead exploited the spatial resolution and sensitivity gains afforded by high laser repetition rate combined with efficient aerosol transfer. The new method successfully mapped trace elements at single to double digit ppm levels and the maps reveal fine-scale zoning of trace elements with an effective x and y resolution of 5 μm, while white light interferometry showed that for each experiment only ca. 1 μm of sample was removed. Repeated mapping of the same area showed excellent correspondence not only between element concentrations in successive experiments but also in the shape, dimension and location of regions on interest defined with concentration criteria. The very good repeatability of the elemental maps indicates that for studies requiring more analytes, successive mapping of additional elements is possible. By contrast with conventional very small spot (i.e. 5 μm) analysis, fast repetition rate and stage scan speed mapping avoids down-hole fractionation effects and minimizes accidental analysis of buried invisible inclusions. Compared to conventional LA-ICP-MS mapping, the method reduces the experiment time by 4-8 times.

Introduction

The minor and trace element composition of minerals provides critical insights into a variety of geological processes including the passage of magma and crystals in volcanic plumbing systems (Ubide and Kamber 2018; Magee et al. 2020); the nature, origin, and evolution of ore-forming fluids (Pfaff et al. 2011; Cook et al. 2013); changes in pore water fluid composition during diagenesis (Gregory et al. 2019); and oxidation-reduction conditions in paleo-oceans (Large et al. 2014; Gallagher et al. 2015; Mukherjee et al. 2019). Furthermore, the presence and distribution of minor and trace elements can have important implications for understanding mineral processing and environmental management requirements (e.g. Parbhakar-Fox et al. 2013; Sykora et al. 2018). Laser-ablation inductively-coupled-plasma mass-spectrometry (LA-ICP-MS) has proven particularly useful in documenting the behavior of elements that substitute into the lattice of sulfide minerals (Large et al. 2007; Ulrich et al. 2011) or form exsolved monosulfide solution minerals (Ulrich et al. 2009; Cafagna and Jugo 2016; Duran et al. 2016). Methodological improvements have been rapid (Heinrich et al. 2003; Günther and Hattendorf 2005; Sylvester 2008; Cook et al. 2016) and now permit the use of increasingly small laser beam diameters, dropping from 50-70 μm in the past to as low as 5 μm applied today (Sylvester and Jackson 2016). As the spatial resolution of the method continues to improve, increasingly complex internal element zonation has been revealed in many minerals (Ingham et al. 2014), including igneous silicates, phosphates and particularly sulfides (e.g. Zhou et al. 2017).

In the simplest case, the internal heterogeneity in trace element distribution within a mineral is broadly concentric (Gallagher et al. 2015) and can be adequately documented with line scans across the mineral (Gadd et al. 2016). However, intricate patterns including corroded 'cores', nuggets, oscillatory and sectorial zoning, and 'fractures' have been documented in sulfides

(Large et al. 2007, 2009; Ulrich et al. 2009, 2011; Genna and Gaboury 2015; Cook et al. 2016; Neyedley et al. 2017; Zhu et al. 2021). Two-dimensional semi-quantitative (SQ) trace element maps are therefore increasingly used to provide a chemical context for further in situ analysis. One common approach is to produce a small number of element maps of representative sample areas to guide spot selection and analyses (e.g., Gregory et al. 2016), the other is to produce maps for the full crystals of interest without additional spot analyses.

One significant ambition of LA-ICP-MS analysts is to move from spot analysis guided by qualitative maps towards quantitative mapping (Paul et al. 2014; Petrus et al. 2017) where the analyst retrospectively selects regions of interest (ROI) after data acquisition. Quantitative mapping holds several potential advantages including that ablation for a map only removes a small amount (depth) of sample. This results in negligible down-hole fractionation (Chew et al. 2017), avoids analyzing material well below the visible surface, and preserves the specimen for additional analysis. Furthermore, data from chemical zones that are irregularly shaped and, therefore inaccessible to larger spot analysis with a square or circular beam aperture, can be pooled during post-processing to improve counting statistics (Gadd et al. 2016; Petrus et al. 2017; Stead et al., 2017). Finally, concentration data from maps can be interpreted in the context of trace element distribution patterns that are commonly complex but can be cryptic in petrographic or backscattered electron imagery. Interpretation of spot analysis data in such settings can be difficult (Ulrich et al. 2011). Alternative methods such as gamma-enhancement of reflected light imagery (Zhu et al. 2021) or the destructive practice of acid etching (Rickard 2012; Gregory et al. 2015) allow for a general assessment of the spatial distribution of compositional heterogeneities in sulfide grains, but they do not permit the determination of the chemical composition.

Large et al. (2009) were amongst the first to demonstrate successful semi-quantitative imaging of trace elements by LA-quadrupole (Q)-ICP-MS. These authors used a fast-sweeping MS to uncover the distribution of up to 20 analytes in pyrite. The acquisition of many elements on a sequential mass analyzer results in relatively long collective dwell times (i.e. >0.5 seconds), which limits the speed at which the stage can be moved under the laser to avoid blurring of the resulting map in the stage travel direction. The spatial resolution of LA-ICP-MS elemental mapping is also limited by the washout characteristics of the ablation cell and transfer tubing. Thus, there is a trade-off between the number of analytes acquired, the diameter of the employed beam, the limits of detection and the time it takes to obtain the map. This typically means that high spatial resolution maps, which reveal fine detail, take many hours to acquire (Ingham et al. 2014; Neyedley et al. 2017; Ubide and Kamber, 2018). Some of these limitations can be overcome with mass spectrometers that are capable of simultaneous analyte acquisition: Mattauch-Herzog-MS equipped with a simultaneous (e.g. direct charge) detection system (Wang et al. 2013) and Time-of-Flight-(TOF)-ICP-MS (Gundlach-Graham et al. 2015). However, such instruments are still quite experimental, relatively rare and comparatively expensive, and the limited data from them to date suggest that for the lighter elements (Bussweiler et al. 2020), they cannot currently match the limits of detection achieved when mapping a small number of analytes by Q-ICP-MS.

Until recently, there were three fundamental limitations to quantitative LA-ICP-MS mapping. First, the speed of the method was critically limited by a feature of conventional instrumentation: the slow washout time of aerosols in the ablation cell severely restricted the maximum stage scan speed during imaging experiments. This made the production of element maps slow and required large amounts of expensive consumables (carrier and plasma gases).

Second, high spatial resolution maps (i.e. <20 μm) have proven difficult to obtain for low concentration elements due to limits of quantification. Third, there was limited availability of software to extract fully quantitative data from trace element maps. However, significant progress has been made in recent years to overcome the first and third of these limitations.

With regards to the first limitation, new devices have been introduced that significantly reduce washout time. For example, Wang et al. (2013) and Gundlach-Graham et al. (2015) used a 'tube cell' that permits resolution of individual pulses fired at 20-30 Hz. The latest low-dispersion LA systems now combine tube cells contained in complex air-tight chambers and achieve >100 Hz pulse resolution (Van Malderen et al. 2020). An alternative and equally effective solution is the commercially available Aerosol Rapid Introduction System (ARIS; Van Acker et al. 2016) used in this study. It consists of a capillary tube and an Ar-He mixing device that permits resolution of 40 to 60 Hz individual pulses. It works with any HelEx II cell-equipped laser ablation system and does not require a low dispersion sample chamber.

Concerning the third limitation of extracting quantitative data from the multi-dimensional x-y-elemental pixel arrays, new software solutions have been proposed. The first such software released addressed the problem that LA-ICP-MS maps commonly cover minerals with different and/or variable internal standard concentrations and was developed in the data reduction software Iolite (Woodhead et al. 2007; Hellstrom et al. 2008). Paul et al. (2014) proposed an algorithm that can distinguish minerals to allow the application of different internal standard concentration. More recently, Petrus et al. (2017) developed a software that can extract pixels from complexly shaped areas of similar chemistry in SQ maps, which can be turned into fully quantitative data if the concentration of an internal standard is known for a ROI via an independent method of analysis. Another software solution uses multivariate statistics, including

139 principal component analysis, to inspect the full pixel arrays that make up maps (Winderbaum et
140 al. 2012; Gadd et al. 2016). In this approach, statistical measures are used to identify elements
141 that show strongly related or anti-correlated behavior, without attempting to extract data from a
142 particular region on the map.

143 The aim of this study was to address the second limitation: the compromise between
144 spatial resolution, detection limit and overall experiment duration by employing the ARIS with a
145 new set of operating conditions. The ARIS LA-Q-ICP-MS maps for pyrite/marcasite were
146 obtained at much higher laser repetition rates than in traditional experiments, using continuous
147 stage travel at fast speeds and lower laser fluence (Table 1) to avoid ablating deep trenches and
148 melting of sulfides. The limitation of this approach is that it cannot produce maps for more than
149 5-10 analytes per experiment. As a potential work-around, multiple repeat experiments were
150 performed over the same mapping area to test how accurately repeat maps could reproduce x-y-
151 element concentration arrays and ROIs defined on them objectively with element concentration
152 criteria.
153

154 ## Methods and Materials

155 ### Instrumentation: ARIS LA-Q-ICP-MS

156 The instrumentation used in the element mapping experiments was an Analyte G2 193
157 nm excimer ArF laser ablation system equipped with a HelEx II 2-volume cell (Teledyne Photon
158 Machines, Bozeman, MT, USA) coupled to an iCap-Qc Q-ICP-MS (Thermo Scientific, Bremen,
159 Germany). It was retrofitted with a Teledyne Photon Machines ARIS, which connected the
160 ablation cell to the ICP-MS torch. The ARIS is a high-speed aerosol transfer tubing system that
161 reduces ablation aerosol washout times by up to 2 orders of magnitude compared with

conventional ablation cell-transfer tubing configurations. It also uses a connector piece with which an Ar carrier sheath is created around the central He ablation gas to inject ablated particles into a more confined central area of the plasma. When used in spot analysis mode, the ARIS has been shown to produce accurate trace element data at sub-ppm concentrations (e.g. light rare earth elements in garnet and olivine; Petrus et al., 2017 and Stead et al., 2017, respectively) and U/Pb zircon age data (Chew et al., 2017) at 40-80 Hz laser repetition rates.

With the ARIS, the washout time depends on the length and diameter of the transfer tube. For a comfortable fit between the laser ablation unit and the mass spectrometer, the length of tubing typically needed results in a washout time of ca. 20 ms. For the experiments reported here, the shortest possible tubing (700 mm long, 0.75 mm internal diameter) was used. This setup yielded a washout time of 15 ms and individual ablation pulses could be resolved at sampling rates up to 50-60 Hz, depending on beam diameter and sample material. However, the very short connection prevented the laser ablation system from being able to access the full area of the cell. By comparison, conventionally configured LA-ICP-MS systems have washout times of up to 1-2 s which results in the overlap of single pulse responses at sampling rates exceeding 1-2 Hz. Two-volume cells using minimal smoothing can achieve 90% washout times of ca. 250 ms (Chew et al. 2017).

The capability of the ARIS prototype technology was initially demonstrated by imaging element distribution in semi-conductors (Van Malderen et al. 2015), in biological tissues (Van Malderen et al. 2016) and in conjunction with an ICP-TOF-MS on very fine-grained petrology experimental charges (Bussweiler et al. 2020). Importantly, in these applications, 'spot-resolved' images were created by moving the stage exactly 1 width of the beam between each laser pulse and recording the response from each pulse with very short acquisition times (<1 ms) on the Q-

ICP-MS or by integrating >1,000 TOF-MS mass spectra corresponding to one pixel. The resulting image is essentially an array of adjacent single shot spot analyses (Fig. 1A). Conventional ablation cell configurations made spot-resolved imaging at high resolution or for large areas very time-consuming. Although having a significant speed advantage, the serious limitation of the ARIS spot-resolved approach for systems equipped with a Q-ICP-MS is that the very short acquisition times limits its application to one or two analytes of interest.

In this study, we trialed the ARIS with operating conditions modified from the original purpose (i.e. the spot-resolved approach). Rather, we wanted to explore its utility in continuous signal acquisition for high resolution multi-element mapping of minor and trace components in geological samples with a very small beam size. The components of the analytical philosophy were: to use a small 5 μm beam aperture capable of resolving fine-scale compositional detail; to use the highest washout-permissible repetition rate of 50 Hz to increase the size of the signal; to move the stage with a fast scan speed of 40 μm s^{-1}; and to limit excessive ablation depth by lowering the fluence to 1.0 J cm^{-2}, close to the ablation threshold for silicate glass. For comparison, the construction of a 1,000 x 1,000 μm map with a 5 μm beam and a stage travel speed of 5 μm s^{-1} takes 11.1 h (Ingham et al. 2014) without any beam overlap or pause between line acquisition. Using the parameters tested here, the experiment time would be reduced 8-fold to 1.4 h.

In trials performed ahead of the reported experiments, we initially evaluated the smallest (10 μm) square aperture available on the LA unit but found that relative to the width of chemical zonation in the studied material, a smaller aperture size was needed. Instead, the experiments were performed with a fixed round 5 μm aperture and the distance between adjacent lines of the mapping area was set at 4.5 μm (somewhat less than the nominal beam diameter) as

recommended by Ubide et al. (2015) for circular apertures, resulting in lines of slightly overlapping ablation craters. A 10 s pause in sampling between ablation lines ensured that the gas flows stabilized between line acquisitions and that there was a complete absence of mixing from line to line, either within the sample or between the sample and the standard. The map area was 450 µm wide by 350 µm long and the experiment lasted 0.8 h with an additional 2 m at the start an end for the reference material analyses.

In our experiments, with 700 mm long of 0.75 mm internal diameter transfer tubing, the aerosol was transported with a total He gas flow of 0.35 l min^{-1} (less than half of typical He flow rates) that was supplied in ca. 50:50 proportion to the cell body and the cup. With the ARIS device, the Ar carrier gas is not added in a mixing 'bulb' but at the end of the transfer tubing through the adapter to create a sheath-like Ar flow carrying the particles in the He. As with conventional aerosol transfer, Ar (0.6 l min^{-1}) and high-purity N_2 (11 ml min^{-1}) gas flows are adjusted to achieve best sensitivity at a Th/U ratio of 1.0 and a ThO^+/Th^+ formation rate of 0.1 to 0.2%.

Because the ARIS delivers the aerosol more centrally into the plasma, the expansion chamber pressure of the ICP-MS was on average 0.2 mbar higher than with conventional transfer. Despite the reduced He flow (i.e. 0.35 l min^{-1}), compared to routine operation (0.7 to 1.0 l min^{-1}), we attribute this observation to higher transfer of He through the sample cone and the difficulty of pumping He from the expansion chamber. In terms of total signal size, the direct comparison between routine vs. ARIS mode showed a substantial overall increase with the ARIS. In our Q-ICP-MS, we found that the lower mass range benefitted more (up to 2-3 x) in signal increase than the heaviest mass range (from 1.5-2 x) with additional signal mainly found by the greater MS tuning flexibility afforded by the lower He and Ar gas flows from the ARIS.

Substantially improved ion yields for small spot laser ablation with the ARIS have also been reported for multi-collector ICP-MS (Craig et al. 2018) particularly for the high mass range. Finally, the overall intensity gains did not come at a cost of elevated signal backgrounds with the ARIS installed. As reported with earlier data from this instrument setup (e.g. Stead et al. 2017) for silicates, backgrounds on interference-free masses (e.g. many of the REE and the actinides) remained at the 0.5-2 cps, typical for the iCap-Qc Q-ICP-MS. Combined with the improved wash-out characteristics of the ARIS, this resulted in at least 10-fold improvement in signal/noise ratios over conventional spot LA-Q-ICP-MS on interference-free masses.

Mass spectrometry

The mass spectrometer data was acquired with Qtegra2.2 software (Thermo Scientific, Bremen, Germany) in time-resolved mode. During each experiment, the mass spectrometer scanned for an Fe isotope and 5 trace element isotopes, each with an acquisition time of 20 ms yielding a total dwell time of 120 ms. In the selected configuration (i.e., the combination of gas flows, stage travel and repetition rate), 20 ms was the shortest acquisition time that yielded a signal of acceptable (±20%) stability. Because the total dwell time affects the map resolution in the stage travel direction it is not possible to obtain data for a large number of analytes if high-resolution mapping is the ultimate goal.

To attempt to overcome this limitation, the same area was mapped in three consecutive experiments, taking advantage of the excellent x-y stage reproducibility of the laser ablation system. To ensure optimal ablation, the beam was re-focused on the freshly ablated surface before repeating the experiment. Several trace elements (As, Sb, Tl, and Pb) were repeated in the third experiment to enable comparisons of element maps obtained in unrelated earlier experiments. Analytes mapped were as follows:

Experiment 1: ^{58}Fe, ^{59}Co, ^{60}Ni, ^{73}Ge, ^{75}As, ^{95}Mo

Experiment 2: ^{58}Fe, ^{77}Se, ^{107}Ag, ^{121}Sb, ^{205}Tl, ^{208}Pb

Experiment 3: ^{58}Fe, ^{75}As, ^{121}Sb, ^{197}Au, ^{205}Tl, ^{208}Pb

Data reduction and quantification

The laboratory had access to a set of silicate reference materials, including NIST 610 and 612 but in terms of sulfide (glasses) we could only secure the synthetic polymetallic sulfide pressed pellet MASS-1 at the time of experimentation. Initial tests with the pressed pellet showed that it did not behave well under high repetition rate ablation. It was found that during high repetition rate and fast stage travel ablation, excess material was removed from the periphery of the ablated line. Resulting ion signals also contained spikes in apparent intensity, interpreted to represent accidentally dislodged, relatively larger particles.

For this reason, NIST 610 was used to produce semi-quantitative (SQ) maps. The main limitation to obtaining meaningful quantitative data with NIST 610 is that Fe is a trace metal in the NIST glasses whereas the target minerals pyrite and marcasite (FeS_2) have a stoichiometric Fe concentration of 46.55 wt%. This created a problem for the selection of the most appropriate Fe isotope to be analyzed. On the one hand, the more abundant ^{57}Fe trips into analogue mode when ablating FeS_2 and on the other hand, the less abundant ^{58}Fe returns a very small signal on NIST 610, additionally interfered by nickel. We opted to avoid the analogue pulse-count factor complexity by analyzing ^{58}Fe, and although the Fe signal was quantifiable, the data reduction resulted in large error on the NIST 610 glass introducing unnecessary internal uncertainty into the data. The Fe signal was thus only used to define masks on maps for Fe-sulfides and the calibration was performed via the As concentration known from electron probe microanalyser (EPMA) data (more details below).

This is the peer-reviewed, final accepted version for American Mineralogist, published by the Mineralogical Society of America.
The published version is subject to change. Cite as Authors (Year) Title. American Mineralogist, in press.
DOI: https://doi.org/10.2138/am-2022-8168. http://www.minsocam.org/

Element distribution maps were processed and compiled with the commercially available software Iolite v3 (Paton et al. 2011), which functions as an add-in for WaveMetrics' IgorPro data analysis program (http://www.wavemetrics.com). Data for minor and trace elements were reduced to yield SQ concentrations with the 'Trace_Element' data reduction scheme (DRS) whereas data for Fe were reduced to yield counts per second with the 'Baseline_Subtract' DRS, both of which are issued with the Iolite software (Longerich et al. 1996). Element maps were produced with the Iolite module 'CellSpace'(Paul et al. 2012).

Because the composition of Fe sulfide within the mapping area had been measured at various locations with EPMA (details in Appendix A), they were available to calibrate the SQ concentrations in the minor and trace element maps to quantitative values as follows. The average As concentration in 'ppm SQ' units was calculated for circular ROIs ~25 µm in diameter located at the approximate location of each WDS analysis using the Iolite add-in 'Monocle' (Table 2; Petrus et al. 2017). Regions of interest were centered on corresponding EPMA analysis (Fig. 2) but in a few cases the calculated area was adjusted slightly to ensure it contained homogenous concentrations representative of the location of the EPMA analysis. Arsenic was used for calibration because the EPMA results offered a wide range of concentrations above the limits of determination (Table 2).

Linear regression (forced through zero) of the SQ and EPMA data yielded a slope of 2.95 with R^2 of 0.997 and a root mean square error (RMSE) of 244 ppm (Fig. 3). Thus, SQ concentrations overestimated true concentrations by 2.95x, suggesting that at the low fluence applied, ablation rate on sulfide and ion yield from sulfide aerosol was ca. 3x higher than on silicate glass. The apparent concentration of each SQ map was thus adjusted by a factor of 2.95. Although somewhat unorthodox, this process is like the quantification typically undertaken

300 within Iolite in that a single correction factor (i.e., the internal standard) is applied to all analytes.
301 The correction factor was also applied to the limits of detection and quantification for the
302 mapping experiments (Table 3) and the average concentrations for regions of interest within the
303 maps (Tables 4, 5).

304 The corrected scale for element concentration is only accurate for FeS_2 minerals. For this
305 reason, a digital mask hiding non-FeS_2 minerals was overlain on the minor and trace element
306 maps. The masks also served to focus the eye on the structure within FeS_2 and avoid detraction
307 by the complexity in the surrounding minerals. The masks were produced with the Mineral
308 Mapping tool in the 'Baseline_Subtract' DRS, which did an excellent job distinguishing FeS_2
309 from other minerals (sphalerite, quartz) while excluding pixels with low Fe signals.

310 **White Light Interferometry**

311 White Light Interferometry was carried out with a Profilm3D system (Filmetrics Inc., San
312 Diego, CA, USA) on the ablated sample surface to evaluate the depth of ablation removal and
313 differential ablation behavior. Data was acquired and processed using the Profilm3D software
314 and data analysis was completed using the SPIP software package (Image Metrology A/S,
315 Hørsholm, Denmark). Scans were carried out using vertical scanning interferometry (VSI) using
316 an envelope center method to determine the z position and a scan length of 0.15 mm. Individual
317 scans were completed using a 50x magnification optical lens and stitched together into a single
318 scanned image in the Profilm3D software using a 20% overlap. At the beginning of each
319 analytical session a 1.818 μm step-height standard (VLSI standard Inc., Milpitas, CA, USA) was
320 measured to test the scan settings and accuracy to a tolerance of 1.8 ±2% of the nominal standard
321 thickness.

Sample Material

The specimen mapped in this study is from a mineralized sample from the Anarraaq Zn-Pb-Ag deposit, which is located in the Red Dog District of northwestern Alaska, USA (Kelley et al. 2004; Reynolds et al. 2021). The Red Dog District contains multiple clastic-dominated (CD) Zn-Pb deposits and is one of the world's largest producing zinc mines (Blevings et al. 2013). The LA-ICP-MS analytical work was conducted on a small piece of thin-section mounted in an epoxy puck. The map area contains hydrothermal Fe sulfide (pyrite and marcasite; FeS_2) and lesser sphalerite (ZnS), and late-stage quartz and calcite.

The LA-ICP-MS work in this study was conducted after *in situ* S isotopic (secondary ion mass spectrometry; SIMS) data had been acquired (Reynolds 2019). The SIMS analysis left disc-shaped craters 15 μm in diameter and 1-2 μm in depth (Fig. 4). The Au coating used in SIMS analyses was removed with a potassium iodide solution, but the puck was not polished before LA-ICP-MS mapping to avoid potential damage to already very thin samples. As will be shown, the SIMS craters do not correlate with any element concentration anomalies of a similar shape and size.

Results

The overview map (Fig. 4) shows that nine of the minor and trace elements analyzed reach concentrations above the background with complex, but clearly not random, distribution in the Fe sulfide minerals. Maximum concentrations on the maps are as high as 10,000s of ppm Pb (from galena inclusions); 1,000s of ppm Sb, As, Tl, and Ag; 100s of ppm Ni; and up to 10s of ppm Co Ge, and Mo. Results for Se and Au are not displayed because of the lack of counts above background (Se) and because of the potential for contamination from the Au coating used in the SIMS analysis, respectively. Minimum concentrations for most metals in the pyrite

345 approach the limits of detection. Thus, the analyzed pyrite shows extreme contrasts in element
346 concentrations despite its relatively small size (300 μm across). Such stark concentration
347 contrasts over narrow areas are not typically encountered in silicates and illustrates the suitability
348 of sulfides to test the new method of this study. Unmasked versions of element maps are
349 provided in Appendix B.

350 **Validation of concentration quantification method**

351 To validate our approach to quantification, conventional LA-ICP-MS spot analysis was
352 also carried out after mapping and results were compared with the average concentrations
353 calculated for corresponding ROIs on the ARIS-LA-ICP-MS element maps (Table 5). Spot
354 analysis was performed with the same equipment fitted with conventional transfer tubing, and
355 using ^{57}Fe as internal standard and the certified reference material MASS-1 for calibration for all
356 elements. Samples were ablated with a spot size of 20 μm, for 30s with a much slower repetition
357 rate of 10Hz but a much higher energy density of 2-3 J/cm^2. The data was reduced with Iolite 4
358 (Paton et al., 2011) using the Trace Elements DRS (Longerich et al 1996). A more detailed
359 description of the methodology for spot analyses and full results is available in Appendix C.

360 A cross plot of As concentrations determined by spot analysis and calculated for ROIs on
361 the ARIS map (Fig. 5) shows a linear regression with a slope very close to 1 (1.09), with with R^2
362 of 0.584 when the intercept was forced to zero. The proximity of the slope to 1.0 indicates that
363 the concentrations agree, on average, within 10%. However, the goodness of fit is only moderate.
364 This improves substantially after excluding those spot analyses in which the down-hole As signal
365 strongly varied (e.g., Fig. 5c-e). For the dataset excluding inconsistent down-hole As signals, the
366 linear regression forced through zero yields a slope of 1.21 with a much improved R^2 of 0.970. A

This is the peer-reviewed, final accepted version for American Mineralogist, published by the Mineralogical Society of America.
The published version is subject to change. Cite as Authors (Year) Title. American Mineralogist, in press.
DOI: https://doi.org/10.2138/am-2022-8168. http://www.minsocam.org/

second such comparison was carried out for Ag: the linear regression forced through zero yields a slope of 0.918 with R^2 of 0.912 (Fig. 6).

Although the correspondence between map and spot concentrations deviates somewhat from 1.0 (0.918 for Ag and 1.27 for As), the general agreement is much better than the 2.95 factor that was used to convert the SQ map data to quantitative concentrations. Furthermore, the down-hole spot signals reveal the presence of buried micro-inclusions (particularly in As and Sb) whose minor presence will undoubtedly negatively impact any method comparison. In summary, the very good correspondence of the calibrated concentrations on two separate instruments, operated at different conditions suggests that the calibration approach yielded reasonable concentrations in the ARIS-LA-ICP-MS element maps.

The more extensive trace element dataset from the spot analyses also allows to verify the veracity of the elemental maps in terms of molecular interferences. On the unmasked maps (Appendix B) it can, for example, be seen that sphalerite grains adjacent to the FeS_2 phases, show high Ag concentrations. While this likely is a real feature of Ag substitution into sphalerite, the ^{107}Ag signal could contain an undetected molecular interference from Zn-argides (e.g. $^{67}Zn^{40}Ar$) and by analogy, some of the Ag zonation within the FeS_2 phases could instead reflect Zn. Within the spot LA-ICP-MS data, however, there is a complete absence of correlation between Zn and Ag (R^2 of 0.0084). Because the spot and map Ag data agree very well, the possibility of undetected molecular interference contribution to element zonation is considered very small and the presence of Ag in the studied FeS_2 phases is considered real, similar to that reported by Large and Maslennikov (2020).

Limits of detection and quantification

Like conventional spot LA-ICP-MS analysis, the limits of detection (LOD) depend on the signal/noise ratio, the size and stability of the background signal at each mass, the abundance of the isotope analyzed and the mass response curve of the MS. In general, Q-ICP-MS return the best LOD in the mid to high-mass range and for mono-isotopic elements. Unlike conventional spot analysis, LODs for areas extracted from maps also strongly depend on the total number of pixels contributing to a ROI (corresponding to the collective time of integration; see Appendix A of Petrus et al., 2017).

Representative theoretical LODs were calculated for each experiment by averaging line segments 5-7 s in length from ca. 70 lines per map (Table 3). The number of data contained in the chosen segments corresponds to the approximate length of the signal obtained for one traverse across the FeS_2 portion of the maps. Results were divided by the same internal standard correction factor (2.95) as applied to the element maps but without propagating uncertainty of the As analysis. The LODs were highest for Ni and Ge with 4.91 and 1.01 ppm, respectively. For the other minor and trace elements, the LOD were sub-ppm concentrations. Predictably, the mono-isotopic Co and the high-mass Tl returned very low LODs of 0.18 and 0.044-0.070 ppm, respectively, but owing to the very low instrument signal background (for many masses <0.5 cps), most analytes had very low LODs (e.g., Mo and Ag with 0.066 and 0.11 ppm, respectively). For pure visual interrogation of a mineral chemical map, the LOD is the most important factor and determines at which concentration a spatial distribution feature can still be resolved. However, for quantitative mapping, the limits of quantification are relevant. These are listed in Table 3 and depend on the actual size of the recorded signal, the size of the gas and

411 instrumental backgrounds relative to the signal, and the stability of the background. In general,
412 the maps for all analyzed elements show coherent areas of low concentration.

413 The coherence of concentration levels within thin bands of zoning (e.g. As, Tl, Co, and
414 Ni) further illustrates the excellent quality of concentration contrasts captured in the maps. In
415 these elements, individual bands can be recognized that are constituted of very similar along-
416 band concentrations. Of course, the true concentration coherence along a given zone is unknown
417 and there is likely variability within each band but the ability of these maps to show the zonation
418 sharply attests to the sound limits of quantification. We attribute this to the combination of
419 effective signal transfer with the ARIS and very low and stable background signals of the mass
420 spectrometer.

421 **Spatial resolution in x and y for minor and trace elements of limited volatility**

422 In contrast to previous applications of the tube cells of Wang et al. (2013) and Gundlach-
423 Graham et al. (2015) and bi-element maps produced with the ARIS (van Acker et al., 2016), the
424 operating conditions used with the ARIS in this study produce overlapping ablation pulses. This
425 is caused by the deliberate continuous stage travel; the sample area in the center of line scan
426 experiences up to 7 overlapping pulses (Fig. 1B). The acquisition time was lengthened for two
427 reasons. First, by making the acquisition time at least as long as the time between 2 consecutive
428 pulses, a relatively stable signal is generated, allowing the mass spectrometer to acquire data for
429 multiple analytes. Second, the longer integration time allows more counts to accumulate, which
430 lowers the detection limit and makes possible the quantification of lower abundance analytes. In
431 maps that are shot as orthogonal grids from top left to bottom right, the y resolution is the beam
432 diameter; in our experiments this was 5µm. In terms of the x resolution, we hypothesized that
433 with perfect washout, it would be the distance the beam moves during the total dwell time (Fig.

434 1B). By setting the stage travel speed to 40 µm s^{-1}, we aimed for a theoretical x resolution of 4.8
435 µm (8 beam diameters per second travel and 120 ms total dwell time), very close to the y
436 resolution.

437 Results from the experiments are shown in Fig. 4. Interested readers are encouraged to
438 inspect the maps using a computer to zoom into the finer detail. A full-scale version of the Pb
439 map is also shown in Appendix D. The maps were obtained with CellSpace with one pixel
440 created for each sweep of the detector through the 6 analytes. The pixels are the same size and
441 shape as the nominal beam (5µm, circular) and overlap slightly in the x direction because of the
442 difference between the beam diameter and the distance the beam moves during a single sweep
443 through the analytes (4.8 µm); the overlapping area is assigned the average value of the two
444 adjacent pixels. The overlap in the y direction was constant and we expected it to be 0.5 µm but
445 in reality, the software produced very slightly variable overlaps, which can only be appreciated
446 on the inset areas shown on Fig. 4. We attribute this to a computational artefact of using the x-y
447 positions stored in the laser log file to synchronise with the time-resolved ICP-MS signals to
448 compute pixels of a nominal aperture diameter with some y-direction overlap of the lines. These
449 x-y positioning issues are not encountered when maps are constructed from adjacent (e.g. Van
450 Acker et al., 2016; Van Malderen et al., 2020), rather than overlapping laser ablation areas (see
451 Fig. 1). Regardless, these very minor changes in overlap did not result in cumulative offsets or
452 artefacts and did not affect the ability to compare data from consecutive maps.

453 The actual versus theoretical x-y resolution was assessed with the CellSpace maps, where
454 one pixel is 5.0 µm in diameter, i.e. very close to the expected theoretical 4.8 x 5.0 µm
455 resolution. In this regard, it is important that the euhedral pyrite has oscillatory zoning in several
456 elements, most evidently in As, Sb and Tl (Fig. 4). A realistic estimate for the x resolution can be

made in the Sb map, where a prominent near-continuous zone of enrichment ca. 15 µm inside the crystal edge runs sub-parallel to the y axis of the image. Close inspection of the map (see inset in Fig. 4) shows that the zone is commonly defined by a single pixel. The effective width of the zone is unknown (as it cannot be seen on other types of images), but we conservatively estimate the actual x resolution to be between 5-10 µm. Where a similar zone of enrichment in the Tl map runs sub-parallel to the x axis of the image in the outermost part of the euhedral pyrite crystal (Fig. 4, inset), it is again obvious that an effective resolution in y of 5 µm was achieved. In summary, the fast mapping method afforded a conservatively estimated x-y resolution of 5-10 µm for trace elements. Although not the main purpose of this study, the spatial resolution for trace elements that can become major constituents needs to be separately evaluated particularly when the element is volatile. This more complex case is illustrated in the discussion section.

Qualitative comparison of elemental maps across separate experiments

An important objective of this study was to test how reproducible elemental maps from subsequent but independent mapping experiments would be. Ubide et al. (2015) used white light interferometry to show that the x-y reproducibility of modern laser ablation stages is so good that mapping areas could be re-sampled well to within 1 µm. These authors re-mapped the same areas with different laser ablation parameters to understand the effects of repetition rate, beam size, and stage travel speed on the crispness of the resulting image without an ARIS. Next, we tested the reproducibility of an elemental map between two experiments with the same laser ablation parameters. Qualitative visual comparison of two As maps (Fig. 7) shows very good overall correspondence. This includes a zone of high As concentration that runs in a N-S direction roughly mid-way through the map. White light interferometry of the sample surface

This is the peer-reviewed, final accepted version for American Mineralogist, published by the Mineralogical Society of America.
The published version is subject to change. Cite as Authors (Year) Title. American Mineralogist, in press.
DOI: https://doi.org/10.2138/am-2022-8168. http://www.minsocam.org/

after the 3 mapping experiments had been completed shows that slightly less than 3 μm of material was ablated from the Fe sulfide (Fig. 8), or just under 1 μm per experiment.

One of the challenges of comparing results from different experiments of the same area is to pin down the exact same spatial reference during the post-processing of each experiment. By repeating the experiment, each pulse should theoretically perfectly overlay a pulse from the previous experiment. However, because the laser log data (recording time, laser diameter and x-y position of ablation sites) and the MS data (recording the time of signal acquisition and the signal size) are synchronized to the same time manually in Iolite for each experiment, there ends up being a slight offset in how the pixels are spatially referenced during image construction. In CellSpace, this means that although the pixels from all the maps created in a single experiment are perfectly aligned, the location of those pixels relative to the petrographic image will change from experiment to experiment by a few μm. A quantitative comparison, however, is still possible by extracting independent ROIs of the same compositional features from the independent maps. This quantitative comparison is presented in the next section.

Discussion

Spatial resolution in x and y for minor and trace metals that can also be major elements in inclusions or accessory minerals

The x-y resolution is different for major elements and semi-volatile trace metals. The inferior x-resolution is unlikely to be related to washout or signal smearing but most likely caused by re-deposition of ablated material ahead of the following pulses. The issue can initially be visualized in the Fe maps between quartz and sphalerite that surround the euhedral pyrite (Fig. 2). The reflected light and backscattered electron maps attest to the sharpness of the true grain boundaries but where they are near-vertical on the map (i.e. orthogonal to the stage travel

direction), the apparent Fe concentrations are smeared in the x direction over 2-3 pixels (10-15 μm). This is much farther than the sharp zone of slight Sb enrichment, for example. In our ablation cell, this is the aerosol transport direction and we interpret the smearing of the signal to be the consequence of resampling of ablation material in front of the laser beam, namely deposition of sphalerite and quartz-derived ejecta onto pyrite. Where the grain boundary is near horizontal on the map, it is typically narrower and only 2 pixels wide.

The ejecta redeposition explanation is supported by the observations on the Pb distribution maps. Although measured as a trace element in FeS_2, Pb is a major element in galena, which is present as small inclusions locally in the sample (see backscattered electron image in Fig. 4). Down-stream from galena, horizontal streaks of Pb up to 7 pixels in length are found decreasing in concentration from left to right, most notably from along the N-S edge of euhedral pyrite crystal (Fig. 4). This apparent Pb concentration gradient is along the stage travel direction, as would be expected from diminishing ejecta contamination with distance from galena inclusions in the sphalerite. The same effect is also noted where a thin NW-SE oriented veinlet of galena in the center of the euhedral pyrite crystal seems to create a much larger sub-rounded Pb anomaly in the map (Fig. 4). In contrast, where Pb is present in trace amounts in pyrite, the x resolution can be as good as a single pixel (as seen in the N-S feature in the Pb map inset in Fig. 4). Resampling of ablation material seems to be a bigger problem where sphalerite or galena is in contact with Fe sulfide, rather than quartz. This is likely because quartz does not ablate as readily at the low fluence selected to suit ablation of sulfides. The very limited ablation progress on quartz (with the deliberately low fluence) is clearly evident on the post-ablation white light interferometry topography (Fig. 8), where quartz is strongly elevated against adjacent sulfides.

In summary, the resampling artefact on major elements leads to an effective most pessimistic x-y resolution of 10x25 μm, where the larger dimension in x is noticeable in semi-volatile elements such as Pb that tend to create larger ejecta aprons than refractory elements. Although LA-ICP-MS is rarely used for major element mapping, resampling artefacts in an internal standard used to create quantitative maps would affect apparent trace element concentrations, typically by exaggerating trace element concentrations in areas where the concentration of the major element used as an internal standard is diluted by ejecta from a different mineral. Resampling of ejecta is a limitation of LA-ICP-MS analysis, but in mapping mode, the effects of resampling can be evaluated and problem areas can be avoided with setting simple combined maximum/minimum concentration criteria when pooling pixels for quantitative concentration data (Petrus et al. 2017).

Quantitative assessment of repeat map reproducibility

To assess the repeatability of the quantitative concentration maps, the Monocle tool of Petrus et al. (2017) was used to define ROIs and calculate the statistics for As concentration within them (Table 4). First, the map was divided into five broad areas: 'Inner' euhedral pyrite, pyrite 'Rim', pyrite ‘Core’, 'Marcasite 1', and 'Marcasite 2'. Within each broad area, a criterion was set for Monocle to extract all map pixels above or below a certain As concentration (Table 4). The criterion concentration value was refined by inspecting the distribution of concentrations in the live histogram tool and iterative adjustment to determine which cut-off concentration resulted in ROIs that best overlapped the features observed in the element maps. The spatial distribution of these ROIs is shown in Fig. 7 and the statistical summary is reported in Table 4. To test the quantitative correspondence of the As distribution maps, the average concentrations of correlating ROIs are plotted in Fig. 9. The linear regression (forced through zero) yields a

548 slope of 0.996 with R^2 of 0.9997. If not forced through zero, a slope of 0.991 and R^2 of 0.9995
549 still show excellent correspondence. The quality of the fit, and the near 1:1 slope attest to the
550 repeatability of ARIS high-speed mapping and the robustness of the LA-ICP-MS system.
551 The comparison of two independent maps shows that combining elemental maps from
552 several experiments is a viable workaround to overcome the inherent limitation on the number of
553 analytes of the ARIS method. For example, two experiments with one major element and 5 trace
554 elements could be combined to obtain mapping information for 10 unknowns in a fraction (ca.
555 1/4) of the time used by conventional low repetition rate mapping (compare this study with
556 Ingham et al. 2014 in Table 1).
557 **Recommendations for use and caveats of the tested method**
558 The vast majority of in situ trace element analyses in the geosciences are performed by
559 laser ablation systems connected to Q-ICP-MS. They have a significantly long service life and,
560 for the foreseeable future, will remain the mainstay workhorses for this type of analysis
561 regardless of the fact that simultaneous mass analyzers (e.g. TOF-ICP-MS) and very rapid
562 washout laser ablation units (e.g. Van Malderen et al., 2020) offer superior potential for high
563 spatial resolution trace element mapping. The following recommendations and caveats are thus
564 intended for users of conventional LA-Q-ICP-MS systems wanting to acquire high spatial
565 resolution multi-element maps.

566 • The ARIS aerosol transfer system is a simple and cost-effective retrofit for HelEx
567 II cell-equipped laser ablation system. When operated with the narrowest
568 available internal diameter (0.75 mm) and short (700 mm) transfer tubing, it is
569 capable of resolving individual pulses at 40-50 Hz. This permits high spatial
570 resolution mapping (i.e. 5 μm spot), resolving trace element features of <10 μm.

571 To achieve this resolution, it is necessary to position the torch of the ICP-MS as
572 closely as possible to the location of where the aerosol exits the laser ablation
573 system, by-passing any valves and internal gas handling of the system. Users need
574 to be careful with the increased pressure within the ablation chamber caused by
575 the small internal diameter of the transfer tubing and disable any automated gas
576 flushing routines that deploy high flow rates.

577 • The ARIS carries aerosol with less He (e.g. 0.35 to 0.5 l min^{-1}) than conventional
578 transfer systems and its connector typically requires less Ar gas to achieve high
579 sensitivity (Th/U of 1.0 and ThO^+/Th^+ <0.2 %). This gives the analyst additional
580 flexibility in tuning the ICP to maximum sensitivity, by increasing make-up gas
581 N_2, optimizing the z-direction of the torch, lowering the plasma forward power,
582 and working with higher extraction voltage. This results in improved sensitivity
583 on Q- (this study; Stead et al., 2017) and MC-ICP-MS (e.g. Craig et al., 2018)
584 with no detrimental effect on backgrounds or signal/background ratios. However,
585 operators need to be aware that using the ARIS can elevate the interface pressure
586 by ca. 0.2 mbar. Typical ICP-MS control software can abort after plasma start-up
587 if a target interface pressure is not reached within a specified time window. This
588 can be overcome by increasing the time given to reach the target pressure and/or
589 by raising the target pressure to a value still considered safe by the instrument
590 manufacturer.

591 • To achieve acceptable signal stability with the ARIS in the configuration of this
592 study, the minimum analyte acquisition time is 20 ms, regardless of signal size.
593 This limits the number of analytes that can be mapped by LA-Q-ICP-MS in rapid

stage movement mode because the x-direction spatial resolution is a reflection of stage travel time. With larger internal diameter and longer transfer tubing, the minimum acquisition time can be dropped to 5 ms (e.g., Drost et al. 2018) for mapping with larger diameter beams (Zhou et al. 2017). When mapping with small beams and small analyte numbers, the repeat mapping tested in this study can be used to increase the number of analyzed elements, however, this surrenders some of the time advantage gained by the fast mapping.

- Due to the limited number of analytes permissible, it is not feasible to test for the presence of possible isobaric molecular interferences by analyzing multiple isotopes of one element in the mapping experiment. Instead, preliminary experiments to test for such interferences need to be performed as line scans over areas of similar phases that can be sacrificed or by running stationary spot analyses with larger analyte lists in which the relationship between interferent major ion (e.g. Zn) and potential isobar ($^{67}Zn^{40}Ar$ on ^{107}Ag) can be established.
- A specific challenge for high repetition rate mapping on sulfides is to find suitable calibration reference materials. In our experiments MASS-1 did not ablate well at 50 Hz, with irregular ablation track edges and spikes in signal intensities, interpreted to represent dislodged rather than ablated particles. The irregular ablation behavior from the surface of our MASS-1 was likely exacerbated by insufficient humidity control during storage. We agree with Cook et al. (2016) that the paucity of suitable crystalline sulfide and their limited availability are significant factors compromising sulfide trace element studies.

This is the peer-reviewed, final accepted version for American Mineralogist, published by the Mineralogical Society of America.
The published version is subject to change. Cite as Authors (Year) Title. American Mineralogist, in press.
DOI: https://doi.org/10.2138/am-2022-8168. http://www.minsocam.org/

Implications

In this study we used ARIS LA-Q-ICP-MS with a new set of operating conditions to produce high spatial resolution (5-10 μm) trace element distribution maps of pyrite and marcasite. This novel approach has several advantages over conventional multi-element mapping techniques, including:

- Increased speed of mapping – the ARIS LA-ICP-MS produces maps 4-8 times faster than conventional mapping techniques;
- Decreased cost of consumables – the smaller diameter of the ARIS tubing requires less He carrier gas;
- Decreased limits of quantification – the rapid rate of ablation, central injection of aerosol, and low carrier and make-up gas flows increase ICP-MS tuning flexibility yielding improved signal intensity without elevating backgrounds. This results in low limits of quantification from ablation with small laser apertures;
- Increased resolution – the advances of the ARIS enable the use of smaller beam diameters without excessive compromise of speed, cost, or limits of quantification;
- Better sample preservation – less material is removed during mapping, preserving more of the sample for future analyses. This also allows for good reproducibility in consecutive experiments, meaning additional analytes can be mapped (offsetting one limitation of the ARIS method in this study).

The tested approach provides an accessible way to map trace element distribution in geological materials. In combination with other recent developments in the field of LA-ICP-MS, especially

638 the ability to extract quantitative data from element maps (Petrus et al. 2017), this will lead to
639 advances in the understanding of chemical heterogeneities in minerals.

640 **Acknowledgments**

641 Funding for the Anarraaq project was provided by Teck Resources Limited; a Natural
642 Sciences and Engineering Research Council of Canada (NSERC) Collaborative Research
643 Development Grant 452969-13 awarded to Sarah Gleeson, Robert Creaser and Teck Resources
644 Limited; and a NSERC Vanier Scholarship awarded to Merilie Reynolds. The funding for the
645 LA-ICP-MS study came from a Helmholtz-Rekrutierungsinitive 0316 to Sarah Gleeson. Balz
646 Kamber and Cora McKenna acknowledge support from Science Foundation Ireland (SFI) Grant
647 Number 13/RC/2092, co-funded under the European Regional Development Fund.

648

649 **References cited**

650 Blevings, S., Kraft, J., Stemler, J., and Krolak, T. (2013) An overview of the structure,
651 stratigraphy, and Zn-Pb-Ag deposits of the Red Dog District, Northwestern Alaska. In
652 Special Publication 17 pp. 361–387. Society of Economic Geologists.
653 Bussweiler, Y., Gervasoni, F., Rittner, M., Berndt, J., and Klemme, S. (2020) Trace element
654 mapping of high-pressure, high-temperature experimental samples with laser ablation
655 ICP time-of-flight mass spectrometry – Illuminating melt-rock reactions in the
656 lithospheric mantle. Lithos, 352–353, 105282.
657 Cafagna, F., and Jugo, P.J. (2016) An experimental study on the geochemical behavior of highly
658 siderophile elements (HSE) and metalloids (As, Se, Sb, Te, Bi) in a mss-iss-pyrite system
659 at 650 °C: A possible magmatic origin for Co-HSE-bearing pyrite and the role of
660 metalloid-rich phases in . Geochimica et Cosmochimica Acta, 178, 233–258.
661 Chew, D.M., Petrus, J.A., Kenny, G.G., and McEvoy, N. (2017) Rapid high-resolution U–Pb
662 LA-Q-ICPMS age mapping of zircon. J. Anal. At. Spectrom., 32, 262–276.
663 Cook, N., Ciobanu, C., George, L., Zhu, Z.-Y., Wade, B., and Ehrig, K. (2016) Trace Element
664 Analysis of Minerals in Magmatic-Hydrothermal Ores by Laser Ablation Inductively-
665 Coupled Plasma Mass Spectrometry: Approaches and Opportunities. Minerals, 6, 111.
666 Cook, N.J., Ciobanu, C.L., Meria, D., Silcock, D., and Wade, B. (2013) Arsenopyrite-Pyrite
667 Association in an Orogenic Gold Ore: Tracing Mineralization History from Textures and
668 Trace Elements. Economic Geology, 108, 1273–1283.
669 Craig, G., Managh, A.J., Stremtan, C., Lloyd, N.S., and Horstwood, M.S.A. (2018) Doubling
670 Sensitivity in Multicollector ICPMS Using High-Efficiency, Rapid Response Laser
671 Ablation Technology. Analytical Chemistry, 90, 11564–11571.

672 Drost, K., Chew, D., Petrus, J.A., Scholze, F., Woodhead, J.D., Schneider, J.W., and Harper,
673 D.A.T. (2018) An Image Mapping Approach to U-Pb LA-ICP-MS Carbonate Dating and
674 Applications to Direct Dating of Carbonate Sedimentation. Geochemistry, Geophysics,
675 Geosystems, 19, 4631–4648.
676 Duran, C.J., Barnes, S.-J., and Corkery, J.T. (2016) Trace element distribution in primary
677 sulfides and Fe–Ti oxides from the sulfide-rich pods of the Lac des Iles Pd deposits,
678 Western Ontario, Canada: Constraints on processes controlling the composition of the ore
679 and the use of pentlandite compositions in exploration. Journal of Geochemical
680 Exploration, 166, 45–63.
681 Gadd, M.G., Layton-Matthews, D., Peter, J.M., and Paradis, S.J. (2016) The world-class
682 Howard's Pass SEDEX Zn-Pb district, Selwyn Basin, Yukon. Part I: trace element
683 compositions of pyrite record input of hydrothermal, diagenetic, and metamorphic fluids
684 to mineralization. Mineralium Deposita, 51, 319–342.
685 Gallagher, M., Turner, E.C., and Kamber, B.S. (2015) In situ trace metal analysis of
686 Neoarchaean – Ordovician shallow-marine microbial-carbonate-hosted pyrites.
687 Geobiology, 13, 316–339.
688 Genna, D., and Gaboury, D. (2015) Deciphering the Hydrothermal Evolution of a VMS System
689 by LA-ICP-MS Using Trace Elements in Pyrite: An Example from the Bracemac-
690 McLeod Deposits, Abitibi, Canada, and Implications for Exploration. Economic
691 Geology, 110, 2087–2108.
692 Gregory, D., Mukherjee, I., Olson, S.L., Large, R.R., Danyushevsky, L.V., Stepanov, A.S.,
693 Avila, J.N., Cliff, J., Ireland, T.R., Raiswell, R., and others (2019) The formation
694 mechanisms of sedimentary pyrite nodules determined by trace element and sulfur
695 isotope microanalysis. Geochimica et Cosmochimica Acta, 259, 53–68.
696 Gregory, D.D., Large, R.R., Halpin, J.A., Baturina, E.L., Lyons, T.W., Wu, S., Danyushevsky,
697 L., Sack, P.J., Chappaz, A., Maslennikov, V.V., and others (2015) Trace Element Content
698 of Sedimentary Pyrite in Black Shales*. Economic Geology, 110, 1389–1410.
699 Gregory, D.D., Large, R.R., Bath, A.B., Steadman, J.A., Wu, S., Danyushevsky, L., Bull, S.W.,
700 Holden, P., and Ireland, T.R. (2016) Trace Element Content of Pyrite from the Kapai
701 Slate, St. Ives Gold District, Western Australia*. Economic Geology, 111, 1297–1320.
702 Gundlach-Graham, A., Burger, M., Allner, S., Schwarz, G., Wang, H.A.O., Gyr, L., Grolimund,
703 D., Hattendorf, B., and Günther, D. (2015) High-Speed, High-Resolution, Multielemental
704 Laser Ablation-Inductively Coupled Plasma-Time-of-Flight Mass Spectrometry Imaging:
705 Part I. Instrumentation and Two-Dimensional Imaging of Geological Samples. Analytical
706 Chemistry, 87, 8250–8258.
707 Günther, D., and Hattendorf, B. (2005) Solid sample analysis using laser ablation inductively
708 coupled plasma mass spectrometry. TrAC - Trends in Analytical Chemistry, 24, 255–
709 265.
710 Heinrich, C.A., Pettke, T., Halter, W.E., Aigner-Torres, M., Audétat, A., Günther, D.,
711 Hattendorf, B., Bleiner, D., Guillong, M., and Horn, I. (2003) Quantitative multi-element
712 analysis of minerals, fluid and melt inclusions by laser-ablation inductively-coupled-
713 plasma mass-spectrometry. Geochimica et Cosmochimica Acta, 67, 3473–3497.
714 Hellstrom, J., Paton, C., Woodhead, J.D., and Hergt, J.M. (2008) Iolite: software for spatially
715 resolved LA-(quad and MC) ICPMS analysis. Mineralogical Assoc. Canada Short Course
716 Series, 40, 343–348.

Ingham, E.S., Cook, N.J., Cliff, J., Ciobanu, C.L., and Huddleston, A. (2014) A combined chemical, isotopic and microstructural study of pyrite from roll-front uranium deposits, Lake Eyre Basin, South Australia. Geochimica et Cosmochimica Acta, 125, 440–465.

Kelley, K.D., Dumoulin, J.A., and Jennings, S. (2004) The Anarraaq Zn-Pb-Ag and Barite Deposit, Northern Alaska: Evidence for Replacement of Carbonate by Barite and Sulfides. Economic Geology, 99, 1577–1591.

Large, R., Maslennikov, V., Robert, F., Danyushevsky, L., and Chang, Z. (2007) Multistage sedimentary and metamorphic origin of pyrite and gold in the giant Sukhoi Log deposit, Lena Gold Province, Russia. Economic Geology, 102, 1233–1267.

Large, R.R., and Maslennikov, V.V. (2020) Invisible Gold Paragenesis and Geochemistry in Pyrite from Orogenic and Sediment-Hosted Gold Deposits. Minerals, 10, 339.

Large, R.R., Danyushevsky, L., Hollit, C., Maslennikov, V., Meffre, S., Gilbert, S., Bull, S., Scott, R., Emsbo, P., Thomas, H., and others (2009) Gold and trace element zonation in pyrite using a laser imaging technique: implications for the timing of gold in orogenic and Carlin-style sediment-hosted deposits. Economic Geology, 104, 635–668.

Large, R.R., Halpin, J.A., Danyushevsky, L.V., Maslennikov, V.V., Bull, S.W., Long, J.A., Gregory, D.D., Lounejeva, E., Lyons, T.W., Sack, P.J., and others (2014) Trace element content of sedimentary pyrite as a new proxy for deep-time ocean–atmosphere evolution. Earth and Planetary Science Letters, 389, 209–220.

Longerich, H.P., Jackson, S.E., and Günther, D. (1996) Inter-laboratory note. Laser ablation inductively coupled plasma mass spectrometric transient signal data acquisition and analyte concentration calculation. Journal of Analytical Atomic Spectrometry, 11, 899–904.

Magee, R., Ubide, T., and Kahl, M. (2020) The Lead-up to Mount Etna's Most Destructive Historic Eruption (1669). Cryptic Recharge Recorded in Clinopyroxene. Journal of Petrology, 61.

Mukherjee, I., Large, R.R., Bull, S., Gregory, D.G., Stepanov, A.S., Ávila, J., Ireland, T.R., and Corkrey, R. (2019) Pyrite trace-element and sulfur isotope geochemistry of paleo-mesoproterozoic McArthur Basin: Proxy for oxidative weathering. American Mineralogist, 104, 1256–1272.

Neyedley, K., Hanley, J.J., Fayek, M., and Kontak, D.J. (2017) Textural, Fluid Inclusion, and Stable Oxygen Isotope Constraints on Vein Formation and Gold Precipitation at the 007 Deposit, Rice Lake Greenstone Belt, Bissett, Manitoba, Canada. Economic Geology, 112, 629–660.

Parbhakar-Fox, A., Lottermoser, B., and Bradshaw, D. (2013) Evaluating waste rock mineralogy and microtexture during kinetic testing for improved acid rock drainage prediction. Minerals Engineering, 52, 111–124.

Paton, C., Hellstrom, J., Paul, B., Woodhead, J., and Hergt, J. (2011) Iolite: Freeware for the visualisation and processing of mass spectrometric data. Journal of Analytical Atomic Spectrometry, 26, 2508.

Paul, B., Paton, C., Norris, A., Woodhead, J., Hellstrom, J., Hergt, J., and Greig, A. (2012) CellSpace: A module for creating spatially registered laser ablation images within the Iolite freeware environment. Journal of Analytical Atomic Spectrometry, 27, 700–706.

Paul, B., Woodhead, J.D., Paton, C., Hergt, J.M., Hellstrom, J., and Norris, C.A. (2014) Towards a method for quantitative LA-ICP-MS imaging of multi-phase assemblages: Mineral

identification and analysis correction procedures. Geostandards and Geoanalytical Research, 38, 253–263.

Petrus, J.A., Chew, D.M., Leybourne, M.I., and Kamber, B.S. (2017) A new approach to laser-ablation inductively-coupled-plasma mass-spectrometry (LA-ICP-MS) using the flexible map interrogation tool 'Monocle.' Chemical Geology, 463, 76–93.

Pfaff, K., Koenig, A., Wenzel, T., Ridley, I., Hildebrandt, L.H., Leach, D.L., and Markl, G. (2011) Trace and minor element variations and sulfur isotopes in crystalline and colloform ZnS: Incorporation mechanisms and implications for their genesis. Chemical Geology, 286, 118–134.

Piña, R., Gervilla, F., Barnes, S.-J., Oberthür, T., and Lunar, R. (2016) Platinum-group element concentrations in pyrite from the Main Sulfide Zone of the Great Dyke of Zimbabwe. Mineralium Deposita, 51, 853–872.

Reynolds, M.A. (2019) Sediment-hosted Zn-Pb-Ag mineralization in the Red Dog district, Alaska, USA: pre-ore environments and mineralizing processes. University of Alberta.

Reynolds, M.A., Gleeson, S.A., Creaser, R.A., Friedlander, B.A., Haywood, J.C., Hnatyshin, D., McCusker, J., and Waldron, J.W.F. (2021) Diagenetic Controls on the Formation of the Anarraaq Clastic-Dominated Zn-Pb-Ag Deposit, Red Dog District, Alaska. Economic Geology, 116, 1803–1824.

Rickard, D. (2012) Sulfidic Sediments and Sedimentary Rocks Vol. 65. Elselvier.

Stead, C.V., Tomlinson, E.L., Kamber, B.S., Babechuk, M.G., and McKenna, C.A. (2017) Rare Earth Element Determination in Olivine by Laser Ablation-Quadrupole-ICP-MS: An Analytical Strategy and Applications. Geostandards and Geoanalytical Research, 41, 197–212.

Sykora, S., Cooke, D.R., Meffre, S., Stephanov, A.S., Gardner, K., Scott, R., Selley, D., and Harris, A.C. (2018) Evolution of Pyrite Trace Element Compositions from Porphyry-Style and Epithermal Conditions at the Lihir Gold Deposit: Implications for Ore Genesis and Mineral Processing. Economic Geology, 113, 193–208.

Sylvester, P.J. (2008) LA-(MC)-ICP-MS trends in 2006 and 2007 with particular emphasis on measurement uncertainties. Geostandards and Geoanalytical Research, 32, 469–488.

Sylvester, P.J., and Jackson, S.E. (2016) A brief history of laser ablation inductively coupled plasma mass spectrometry (LA-ICP-MS). Elements, 12, 307–310.

Ubide, T., and Kamber, B.S. (2018) Volcanic crystals as time capsules of eruption history. Nature Communications, 9, 326.

Ubide, T., McKenna, C.A., Chew, D.M., and Kamber, B.S. (2015) High-resolution LA-ICP-MS trace element mapping of igneous minerals: In search of magma histories. Chemical Geology, 409, 157–168.

Ulrich, T., Kamber, B.S., Jugo, P.J., and Tinkham, D.K. (2009) Imaging Element Distribution Patterns in Minerals By Laser Ablation-Inductively Coupled Plasma-Mass Spectrometry (LA-ICP-MS). The Canadian Mineralogist, 47, 1001–1012.

Ulrich, T., Long, D.G.F., Kamber, B.S., and Whitehouse, M.J. (2011) In Situ Trace Element and Sulfur Isotope Analysis of Pyrite in a Paleoproterozoic Gold Placer Deposit, Pardo and Clement Townships, Ontario, Canada. Economic Geology, 106, 667–686.

Van Acker, T., Van Malderen, S.J.M., Van Heerden, M., McDuffie, J.E., Cuyckens, F., and Vanhaecke, F. (2016) High-resolution laser ablation-inductively coupled plasma-mass spectrometry imaging of cisplatin-induced nephrotoxic side effects. Analytica Chimica Acta, 945, 23–30.

Van Malderen, S.J.M., van Elteren, J.T., and Vanhaecke, F. (2015) Development of a fast laser ablation-inductively coupled plasma-mass spectrometry cell for sub-μm scanning of layered materials - Journal of Analytical Atomic Spectrometry (RSC Publishing). Journal of Analytical Atomic Spetrometry, 30, 119–125.

Van Malderen, S.J.M., Vergucht, E., De Rijcke, M., Janssen, C.R., Vincze, L., and Vanhaecke, F. (2016) Quantitative determination and subcellular imaging of Cu in single cells via laser ablation-ICP-mass spectrometry using high-density microarray gelatin standards. Analytical Chemistry, acs.analchem.6b00334.

Van Malderen, S.J.M., Van Acker, T., and Vanhaecke, F. (2020) Sub-micrometer Nanosecond LA-ICP-MS Imaging at Pixel Acquisition Rates above 250 Hz via a Low-Dispersion Setup. Analytical Chemistry, 92, 5756–5764.

Wang, H.A.O., Grolimund, D., Giesen, C., Borca, C.N., Shaw-Stewart, J.R.H., Bodenmiller, B., and Günther, D. (2013) Fast Chemical Imaging at High Spatial Resolution by Laser Ablation Inductively Coupled Plasma Mass Spectrometry. Analytical Chemistry, 85, 10107–10116.

Winderbaum, L., Ciobanu, C.L., Cook, N.J., Paul, M., Metcalfe, A., and Gilbert, S. (2012) Multivariate Analysis of an LA-ICP-MS Trace Element Dataset for Pyrite. Mathematical Geosciences, 44, 823–842.

Woodhead, J.D., Hellstrom, J., Hergt, J.M., Greig, A., and Maas, R. (2007) Isotopic and elemental imaging of geological materials by laser ablation inductively coupled plasma-mass spectrometry. Geostandards and Geoanalytical Research, 31, 331–343.

Zhou, L., McKenna, C.A., Long, D.G.F., and Kamber, B.S. (2017) LA-ICP-MS elemental mapping of pyrite: An application to the Palaeoproterozoic atmosphere. Precambrian Research, 297, 33–55.

Zhu, Q., Cook, N.J., Xie, G., Ciobanu, C.L., Jian, W., Wade, B.P., and Xu, J. (2021) Gamma-enhancement of reflected light images: A rapid, effective tool for assessment of compositional heterogeneity in pyrite. American Mineralogist, 106, 497–505.

List of table & figure captions

Figure 1. Theoretical laser ablation patterns produced with ARIS instrumentation (a) in previous 'spot-resolved' mapping applications and (b) in this study.

Figure 2. Arsenic map from experiment 1 shows the location of EPMA analyses (small solid white circles) and the regions of interest (large open black or white circles). Two scales show the concentration in ppm SQ units and the calibrated equivalent in ppm.

Figure 3. A cross plot of As concentration determined by EPMA and the average As concentration in ppm SQ units calculated for the associated region of interest (ROI) in

844 experiment 1. Error bars represent 2x standard deviation for EPMA results and 2x standard error
845 for ROI calculations.

846 **Figure 4.** Reflected light image, backscattered electron image, and ARIS-LA-Q-ICP-MS
847 element maps. Marcasite is distinguished from pyrite by its pleochroism and darker shade in
848 backscattered electron imagery; spot checks using micro-Raman spectroscopy were used to
849 verify visual identification (for more details, refer to Reynolds et al. 2021). Black circles on
850 reflected light image show locations of LA-ICP-MS spot analysis (more details in Appendix C).
851 All other minerals are masked in all element maps except for Fe. Insets of Sb, Tl, and Pb maps
852 show fine-scale zonation patterns (within dashed black lines) that demonstrate an effective
853 mapping resolution of 1 pixel or 5 μm. A horizontal streak of elevated Pb concentration is
854 attributed to resampling of galena-rich material ablated to the left of the pyrite crystal.
855 Abbreviations: Gn – galena, Mrc – marcasite, Py – pyrite, Sp – sphalerite, Qz – quartz.

856 **Figure 5.** (a) Arsenic concentrations determined by LA-ICP-MS spot analysis are compared with
857 those calculated for the same areas on the ARIS-LA-ICP-MS element map. Inset in (b). Spot
858 analyses in which the As signal varies significantly with depth (e.g., spectra in c and d) are
859 plotted in grey and those with a consistent As signal (e.g., spectrum in e) are in black. Linear
860 regressions are plotted for all data points (dashed line) and for only black data points (solid line).
861 The scale for each analyte signal in c-e has been adjusted for display purposes; these plots do not
862 reflect the true relative concentrations of different analytes.

863 **Figure 6.** Silver concentrations determined by LA-ICP-MS spot analyses are compared with
864 those calculated for the same areas on the ARIS-LA-ICP-MS element map.

865 **Figure 7.** A comparison of As maps produced in experiment 1 (a, c) and experiment 3 (b, d). The
866 ROIs for which pooled statistics were calculated (Table 4) are shown in c and d.

867 **Figure 8.** (a) Reflected light image of sample area after ARIS-LA-Q-ICP-MS experiments. (b)
868 White light interferometry of the same area. Color reflects height of sample surface. Dashed
869 white line in a and b indicates ablated area. (c) Topographic profile from X to Y across ablated
870 area. Abbreviations: Mrc – marcasite, Py – pyrite, Sp – sphalerite, Qz – quartz.

871 **Figure 9.** A cross plot showing the average As concentration for each ROI in experiment 1
872 relative to experiment 3.

873 **Appendices**

874 View here: https://dataverse.scholarsportal.info/privateurl.xhtml?token=9a96bc52-5944-4736-a5c3-
875 bb9647af558f

876 **Appendix A.** Electron probe microanalysis methodology and data.

877 **Appendix B.** Unmasked versions of element maps.

878 **Appendix C.** LA-ICP-MS spot analysis methodology and data.

879 **Appendix D.** Large scale Pb map highlighting resampling streaks.

This is the peer-reviewed, final accepted version for American Mineralogist, published by the Mineralogical Society of America.
The published version is subject to change. Cite as Authors (Year) Title. American Mineralogist, in press.
DOI: https://doi.org/10.2138/am-2022-8168. http://www.minsocam.org/

Table 1. Comparison of LA-Q-ICP-MS analytical protocols of element mapping in pyrite. Note that only the maps produced by Ingham et al. 2014 have a similar resolution to maps in this study.

Author	beam diameter (µm)	repetition rate (Hz)	stage travel speed (µm s^{-1})	fluence (J cm^{-2})	1000 µm x 1000 µm map time* (h)
Large et al. 2009	15 & 25	10	15 & 25	4 to 5	1.2 & 0.4
Ulrich et al. 2011	30	10	30	3 to 4	0.3
Winderbaum et al. 2012	10	10	10 & 20	1.9 to 2.6	2.8 & 1.4
Ingham et al. 2014	5	10	5	NR	11.1
Duran et al. 2015	15 & 25	15	10 & 20	5	1.9 & 0.6
Gallagher et al. 2015	30	10	20	3.2	0.5
Cafagna and Jugo 2016	10	5	10 & 20	5	2.8 & 1.4
Gadd et al. 2016	35 & 50	15 & 25	8	5 to 10	1.0 & 0.7
Gregory et al. 2016	10	10	10	2 to 3.5	2.8
Pina et al. 2016	15	15	12	4 to 6	1.5
Neyedely et al. 2017	20	7	12	6	1.2
This study	5	50	40	1.0	1.4

*Calculated with no overlap or pause between lines.
NR - not reported

This is the peer-reviewed, final accepted version for American Mineralogist, published by the Mineralogical Society of America.
The published version is subject to change. Cite as Authors (Year) Title. American Mineralogist, in press.
DOI: https://doi.org/10.2138/am-2022-8168. http://www.minsocam.org/

Table 2. Comparison of As concentration determined by EPMA and ARIS-LA-ICP-MS with semi-quantitative reduction.

	EPMA		ARIS-LA-ICP-MS Experiment 1	
ID	**As (ppm)**	**2SD**	**As (ppm SQ)**	**2SE**
A	700	29	1850	480
B	800	73	2670	493
C	700	53	1870	336
D	3100	400	8850	6520
E	100	14	154	108
F	2900	740	8910	2050
G	700	92	2010	430

Errors are reported as internal 2 x standard deviation (EPMA) and standard error (LA-ICP-MS).

This is the peer-reviewed, final accepted version for American Mineralogist, published by the Mineralogical Society of America.
The published version is subject to change. Cite as Authors (Year) Title. American Mineralogist, in press.
DOI: https://doi.org/10.2138/am-2022-8168. http://www.minsocam.org/

Table 3. Limits of detection and quantification for analytes measured in mapping experiments. The correction factor of 2.95 has been applied to all values. The error for all analytes is 244 ppm when the error from the calibration curve (RMSE = 244 ppm) is propogated.

	As (ppm)		Co (ppm)	Ge (ppm)	Mo (ppm)	Ni (ppm)	Ag (ppm)	Pb (ppm)		Sb (ppm)		Tl (ppm)	
	Ex. 1	*Ex. 3*	*Ex. 1*	*Ex. 1*	*Ex. 1*	*Ex. 1*	*Ex. 2*	*Ex. 2*	*Ex. 3*	*Ex. 2*	*Ex. 3*	*Ex. 2*	*Ex. 3*
Limits of detection[1]													
Minimum	0.550	0.434	0.0938	0.356	0.000	3.65	0.0646	0.0407	0.0834	0.167	0.155	0.0240	0.0381
Maximum	1.11	1.29	0.277	1.39	0.235	6.28	0.184	0.882	0.986	0.336	0.560	0.0785	0.124
Average	0.743	0.689	0.184	1.01	0.0664	4.91	0.111	0.119	0.317	0.238	0.291	0.0440	0.0699
Standard Deviation	0.132	0.208	0.0420	0.230	0.0570	0.606	0.0231	0.150	0.213	0.0389	0.086	0.0125	0.0211
Limits of quantification[2]													
Minimum	1.75	1.38	0.298	1.13	0.000	11.6	0.205	0.130	0.265	0.530	0.493	0.0762	0.121
Maximum	3.54	4.09	0.880	4.42	0.749	20.0	0.586	2.80	3.14	1.07	1.78	0.250	0.394
Average	2.36	2.19	0.586	3.20	0.211	15.6	0.353	0.379	1.01	0.756	0.926	0.140	0.222
Standard Deviation	0.418	0.660	0.134	0.730	0.181	1.93	0.0736	0.478	0.676	0.124	0.274	0.0397	0.0672

This is the peer-reviewed, final accepted version for American Mineralogist, published by the Mineralogical Society of America.
The published version is subject to change. Cite as Authors (Year) Title. American Mineralogist, in press.
DOI: https://doi.org/10.2138/am-2022-8168. http://www.minsocam.org/

Table 4. Comparison of As composition in ROIs in experiments 1 and 3. The concentration of each ROI is calculated in SQ units and then divided by the correction factor (2.95).

Name of ROI	Criteria for ROI	As (SQ units)		As (ppm)		Area of ROI (μm^2)	
	(SQ units)	*Ex. 1*	*Ex. 3*	*Ex. 1*	*Ex. 3*	*Ex. 1*	*Ex. 3*
Rim - high As	As > 2250	2660(50.5)	2600(47.3)	903(244)	882(244)	2720	n.a.
Rim - low As	As < 2250	1760(42.0)	1760(36.5)	598(244)	595(244)	4153	n.a.
Core	As < 600	277(48.2)	356(29.4)	93.8(244)	121(244)	1038	n.a.
Marc1 - low As	As < 500	269(11.4)	272(11.2)	91.3(244)	92.1(244)	10861	9842
Marc1 - high As	As > 500	816(22.6)	874(24.3)	276(244)	296(244)	11879	12843
Marc2 - low As	As < 500	289(16.6)	308(15.8)	97.8(244)	104(244)	n.a.	3526
Marc2 - high As	As > 500	805(49.3)	745(44.6)	273(244)	253(244)	n.a.	2204
Inner - high As	As > 4500	6780(158)	6750(141)	2297(250)	2286(248)	10612	n.a.
Inner - med As	1800 < As < 4500	3100(63.7)	3130(65.6)	1050(245)	1060(245)	9761	n.a.

Errors are reported as internal 2 x standard error for As (SQ units) and are propogated with the RMSE of the correction factor through to As (ppm). Criteria for ROI were applied to hand drawn areas.

This is the peer-reviewed, final accepted version for American Mineralogist, published by the Mineralogical Society of America.
The published version is subject to change. Cite as Authors (Year) Title. American Mineralogist, in press.
DOI: https://doi.org/10.2138/am-2022-8168. http://www.minsocam.org/

Table 5. Arsenic and Ag concentration determined by traditonal spot analysis compared with average As and Ag concentrations calculated for corresponding regions of interest on the ARIS-LA-ICP-MS map.

	Spot Analyis		ARIS Map		Spot Analyis		ARIS Map	
ID	As (ppm)	2SE	As (ppm)	2SE	Ag (ppm)	2SE	Ag (ppm)	2SE
1	619	79.7	746	71.9	489	56.8	401	163
2	566	83.4	713	70.2	455	52.6	527	188
3	561	56.3	636	51.8	399	79.6	291	219
4	689	124	1248	317	79.5	31.3	61.1	63.4
5	1555	241	2568	350	24.0	3.13	43.9	24.2
6	1137	232	881	274	35.6	7.70	27.5	17.4
7	817	112	1002	165	21.7	4.42	22.6	10.8
8	216	85.2	867	258	17.5	3.26	15.7	12.9
9	863	299	249	98.7	21.9	5.32	21.3	31.9
10	1858	289	543	310	22.2	2.94	17.0	15.7
11	2257	278	2958	451	21.1	3.35	23.9	14.3
12	616	139	1509	338	114	24.1	69.9	110
13	464	62.6	663	46.6	408	75.0	384	195
14	610	80.0	651	54.9	307	37.8	369	123
15	76.6	10.3	123	28.6	190	34.5	109	71.4
16	167	18.0	191	27.5	166	28.3	135	65.6
17	213	25.8	190	18.2	272	38.6	179	82.6
18	83.1	20.6	137	43.3	135	34.8	193	176
19	61.2	15.3	83.0	18.9	45.6	6.88	92.3	72.1
20	148	16.3	176	37.4	21.8	4.25	29.0	14.2
21	238	35.9	310	38.5	12.9	2.35	21.8	8.75
22	234	27.4	214	23.6	12.0	1.05	12.4	6.42
23	145	29.0	216	21.0	15.2	3.58	13.0	8.44
24	168	45.9	255	37.9	13.7	2.58	28.2	27.9

This is the peer-reviewed, final accepted version for American Mineralogist, published by the Mineralogical Society of America.
The published version is subject to change. Cite as Authors (Year) Title. American Mineralogist, in press.
DOI: https://doi.org/10.2138/am-2022-8168. http://www.minsocam.org/

Figure 1

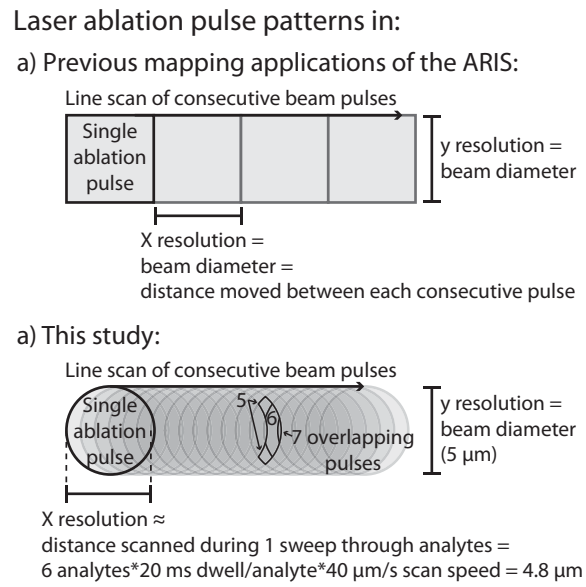

Figure 2

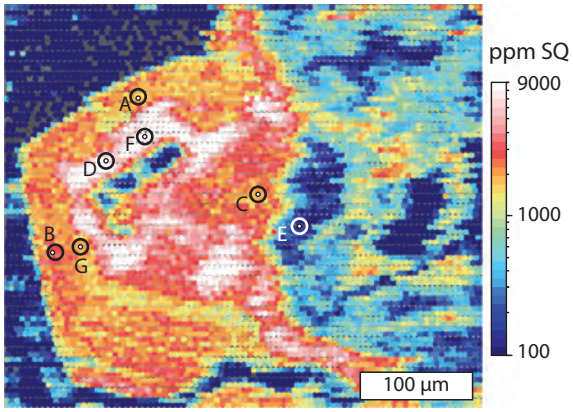

As (Experiment 1)

Figure 3

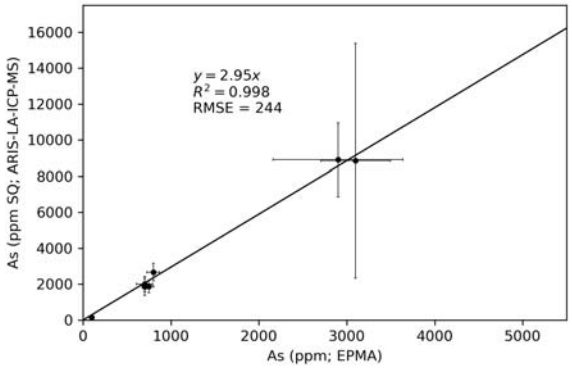

This is the peer-reviewed, final accepted version for American Mineralogist, published by the Mineralogical Society of America.
The published version is subject to change. Cite as Authors (Year) Title. American Mineralogist, in press.
DOI: https://doi.org/10.2138/am-2022-8168. http://www.minsocam.org/

Figure 4

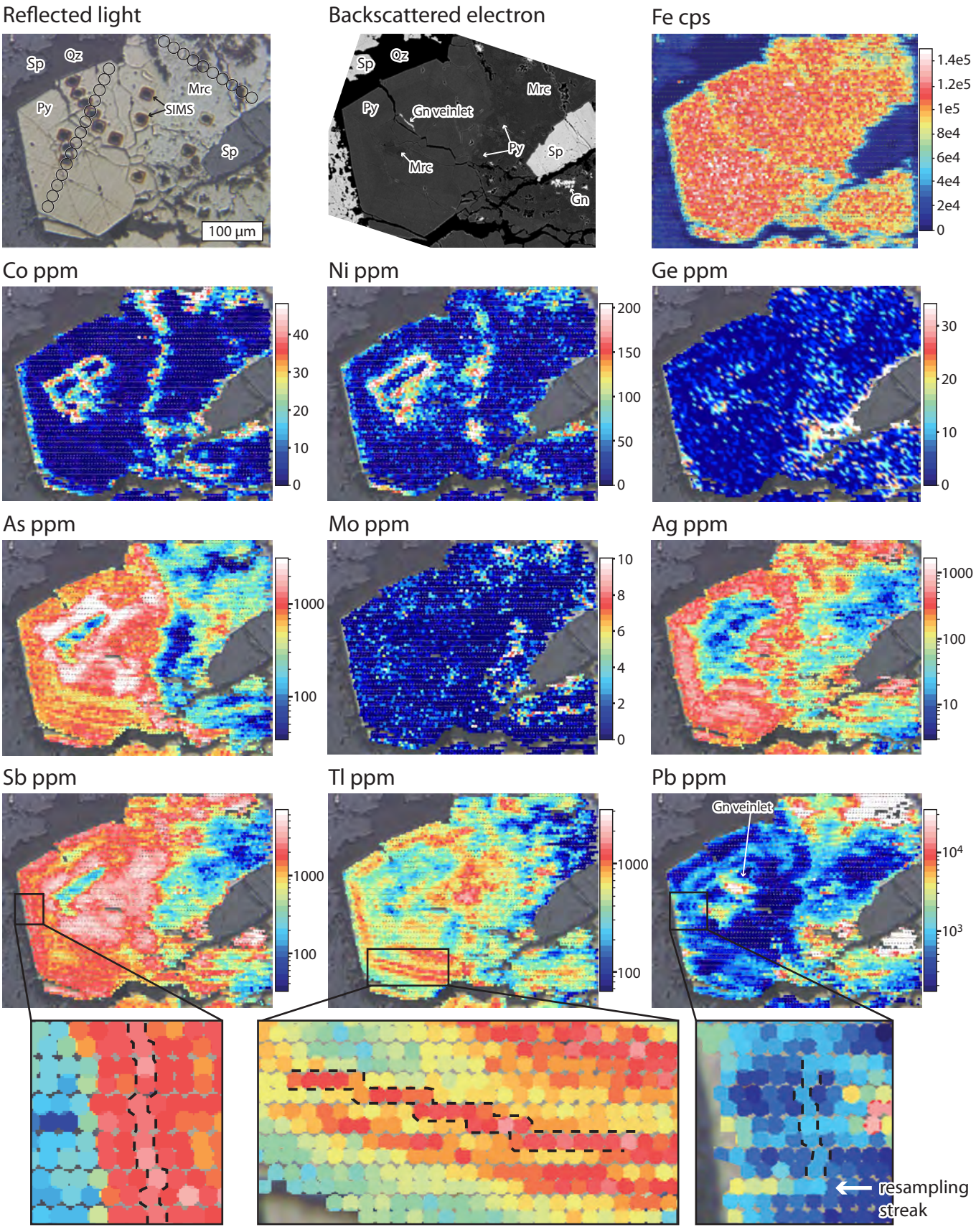

This is the peer-reviewed, final accepted version for American Mineralogist, published by the Mineralogical Society of America.
The published version is subject to change. Cite as Authors (Year) Title. American Mineralogist, in press.
DOI: https://doi.org/10.2138/am-2022-8168. http://www.minsocam.org/

Figure 5

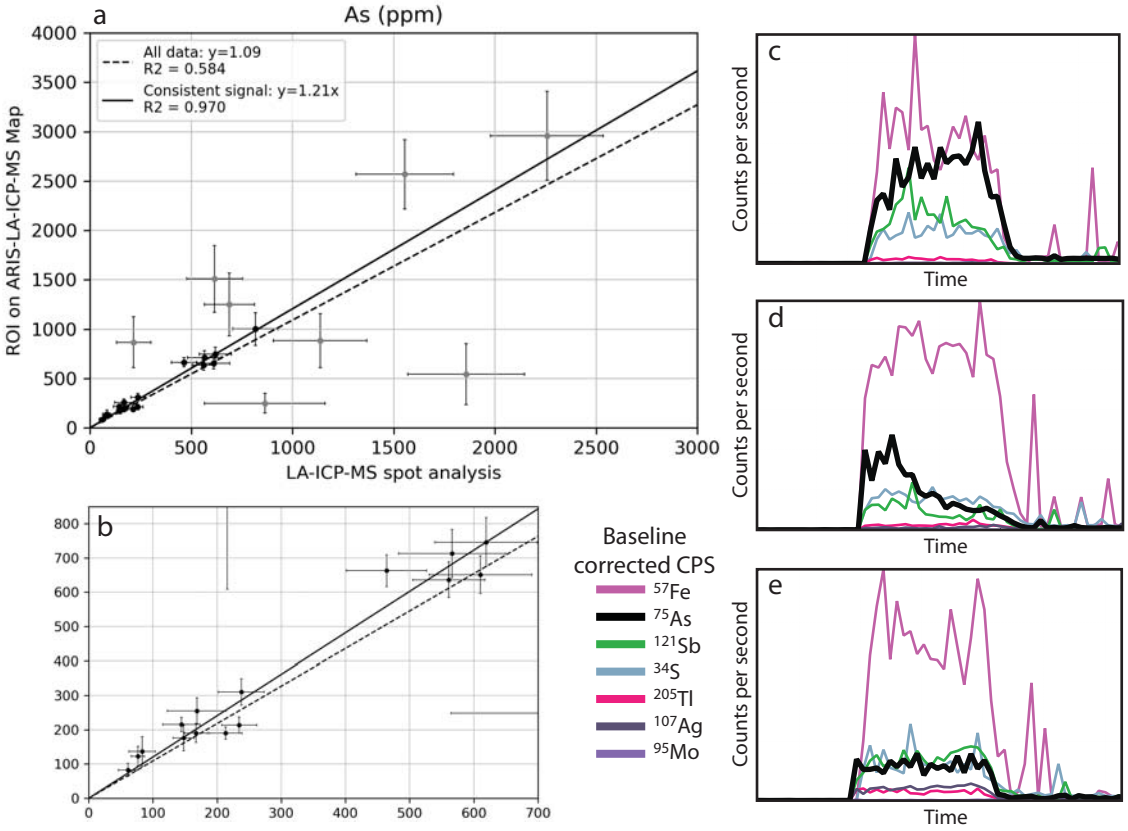

This is the peer-reviewed, final accepted version for American Mineralogist, published by the Mineralogical Society of America.
The published version is subject to change. Cite as Authors (Year) Title. American Mineralogist, in press.
DOI: https://doi.org/10.2138/am-2022-8168. http://www.minsocam.org/

Figure 6

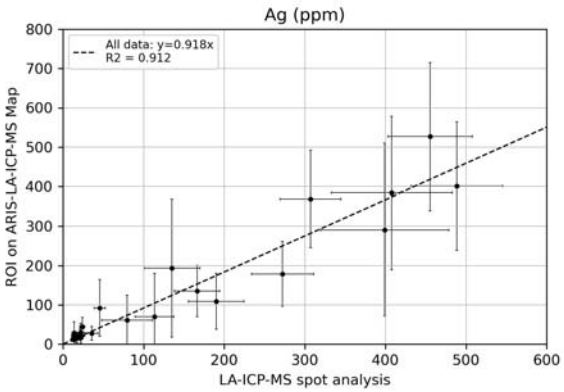

Figure 7

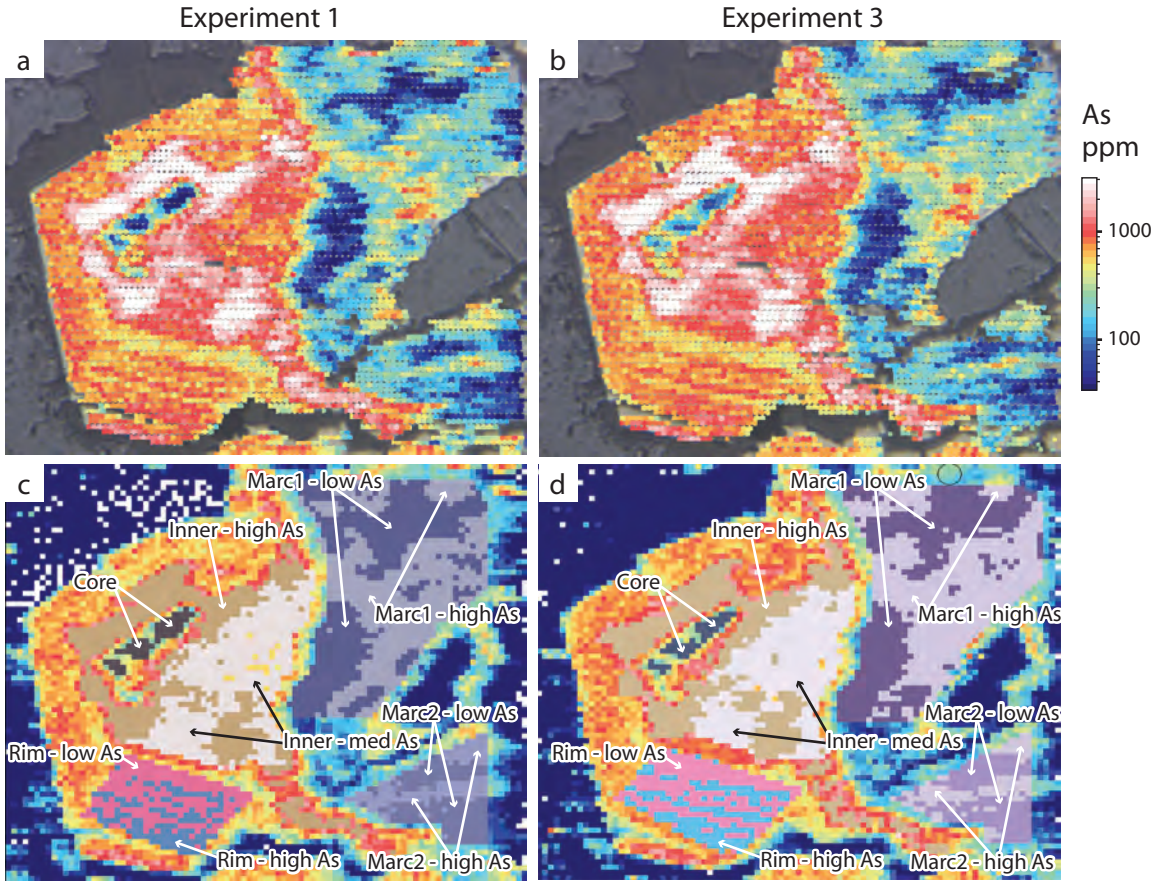

This is the peer-reviewed, final accepted version for American Mineralogist, published by the Mineralogical Society of America.
The published version is subject to change. Cite as Authors (Year) Title. American Mineralogist, in press.
DOI: https://doi.org/10.2138/am-2022-8168. http://www.minsocam.org/

Figure 8

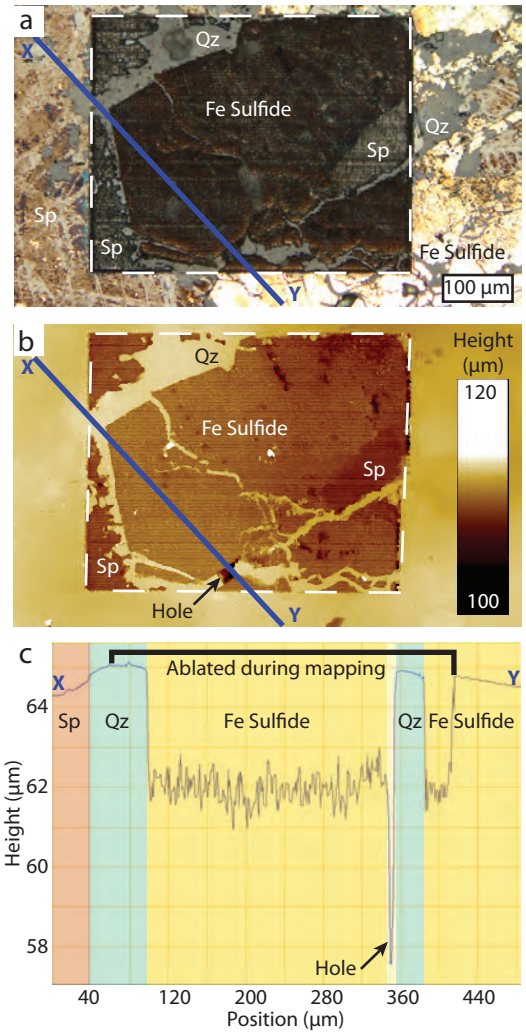

Figure 9